Review of Scientific Instruments

An experiment for novel material thin-film solar cell characterization on sounding rocket flights

Cite as: Rev. Sci. Instrum. **92**, 074501 (2021); https://doi.org/10.1063/5.0047346
Submitted: 12 February 2021 • Accepted: 07 July 2021 • Published Online: 26 July 2021

Lennart K. Reb, Michael Böhmer, Benjamin Predeschly, et al.

Review of Scientific Instruments ARTICLE scitation.org/journal/rsi

An experiment for novel material thin-film solar cell characterization on sounding rocket flights

Cite as: Rev. Sci. Instrum. 92, 074501 (2021); doi: 10.1063/5.0047346
Submitted: 12 February 2021 • Accepted: 7 July 2021 •
Published Online: 26 July 2021

Lennart K. Reb,[1] Michael Böhmer,[2] Benjamin Predeschly,[1] Sebastian Grott,[1] Christoph Dreißigacker,[3] Jörg Drescher,[3] Andreas Meyer,[3] and Peter Müller-Buschbaum[1,4,a)]

AFFILIATIONS

[1] Technische Universität München, Physik-Department, Lehrstuhl für Funktionelle Materialien, James-Franck-Str. 1, 85748 Garching, Germany
[2] Technische Universität München, Physik-Department, Zentrales Technologielabor, James-Franck-Str. 1, 85748 Garching, Germany
[3] Deutsches Zentrum für Luft- und Raumfahrt (DLR), Institut für Materialphysik im Weltraum, Linder Höhe, 51147 Köln, Germany
[4] Heinz Maier-Leibnitz-Zentrum, Technische Universität München, Lichtenbergstr. 1, 85748 Garching, Germany

[a)] **Author to whom correspondence should be addressed:** muellerb@ph.tum.de

ABSTRACT

Novel material thin-film solar cells are promising alternatives to conventional solar cells for future space applications. Previous terrestrial investigations have shown promising stability under simulated space conditions, pioneering the next step to test these solar cells under space conditions. Here, we present the sounding rocket experiment OHSCIS to characterize the electronic behavior of Organic and Hybrid Solar Cells In Space (OHSCIS). The mechanical and electronic design aims at maximizing the rate of data collection and the fail-safety for high scientific output with precise measurements. The maiden flight onboard the MAPHEUS-8 proved the experimental concept to be successful and produced valuable results for the operation and behavior of perovskite and organic solar cells in space.

I. INTRODUCTION

Over the last few years, the technologies of organic[1,2] and hybrid perovskite[3,4] solar cells emerged and have become an increasingly promising research field today. Thanks to their strong rise in power conversion efficiencies[5] and their low weight, they have come to light as an alternative to conventional inorganic solar cells for use in space.[6,7] To investigate their behavior under space conditions, balloon flights and laboratory experiments were conducted with promising results.[8–12] However, terrestrial or near-space solar cell characterization experiments cannot emulate environmental conditions present in orbital altitudes. Sub-orbital sounding rocket flights provide an alternative and elegant platform for such a real-space characterization. The high altitudes reached together with a stabilized payload orientation during micro-gravity (μg) outside of Earth's atmosphere simulate real space conditions for several minutes. This allows conducting several solar cell measurement cycles to study the behavior of these solar cells under extraterrestrial conditions that come closest to their desired application in orbit. Furthermore, the recovery of the experiment after sounding rocket flights opens up the possibility of subsequent investigations of the solar cells. Thus, the OHSCIS sounding rocket experiment has been developed and constructed to characterize Organic and Hybrid Solar Cells In Space (OHSCIS). The maiden flight took place in June 2019 as part of MAPHEUS-8.[13]

The OHSCIS experimental design takes into account all mechanical stability requirements imposed by sub-orbital rocket flights while maximizing the scientific output. This design goal has been realized by incorporating redundancy and resilience to safely collect the utmost reliable high-precision solar cell current–voltage (I–V) data within the limited time of flight. The unusually short development time of less than one year required to reuse already existing working components, concepts, and know-how, while keeping the entire complexity of the system to a minimum level, to

maximize its reliability. The entire experiment features autonomous operation without the need for hookup to onboard communication.

Due to the nondeterministic rocket orientation with respect to the sun during the μg phase, an azimuthal symmetry of the experiment is favored to maximize the probability of solar irradiation on the solar cells. We select an eightfold experiment symmetry as a compromise of maximizing the number of solar cells on the experiment while limiting the number of cut-outs to maintain the structural integrity of the module ring. The cut-outs contain the solar cells and are covered with fused silica glasses to protect the solar cells from heat and stress created during the supersonic ascent and reentry. Typically, three cut-outs are simultaneously irradiated by solar light. This enables the measurement of solar cells of multiple cut-outs to improve the measurement statistics. A high degree of resilience is achieved by partitioning the electronics into eight systems, where each is a self-contained autonomous data-acquisition (DAQ) system. Each DAQ is optimized for a long battery standby time, high-precision low-noise measurements, and high failure safety by including various hardware and software features. Operational tests prove the functionality of the experiment and the solar cell measurement principle. Results of the maiden flight show nominal time-synchronized data acquisition of all eight DAQs during the entire measurement time and successful solar cell I–V measurements during the μg phase.

II. MECHANICAL DESIGN

The experiment is integrated into an anodized aluminum ring with an outer diameter of 438 mm, a height of 170 mm, and a wall thickness of 8 mm. The rather thick wall compensates for structural weakening resulting from the eight cut-outs (hatches). The ring's height is minimized to save weight. In Fig. 1, an oblique-view photograph shows the complete OHSCIS experiment, where different parts are indicated by color. Attached to the inner side of the ring, four stainless steel mounting elbows (green) are attached to the outer structure and center a 3 mm strong aluminum base plate (orange). Stainless steel is chosen here to provide the necessary mechanical strength and to reduce the thermal conduction toward the sensitive electronics, while the aluminum bottom plate works as a heat sink to passively cool the electronics in vacuum. A central cut-out in the bottom plate acts as a cable feedthrough for the communication cable bundle of the service module and other experiments. The eight symmetrically arranged rectangular hatches in the outer ring structure harbor insertion modules (blue). The insertion modules can be mounted and unmounted from the exterior to access the inner experiment and enable solar cell exchange in the assembled payload state before launch.

Each insertion module comprises a fused silica window embedded in two aluminum frames and a solar cell holder, the key part of the insertion module. Figure 2 shows a close-up photograph of the mounted insertion module from the outside. The outer aluminum frame is designed with two continuously varying radii in horizontal and vertical directions to allow for a smooth transition between the cylindrical ring mantle and the flat window to minimize turbulences of the air-flow profile at the rocket surface during supersonic flights and consequently friction and heat. The windows with dimensions of $80 \times 45 \times 4$ mm^3 with small bevels are made of fused silica glass

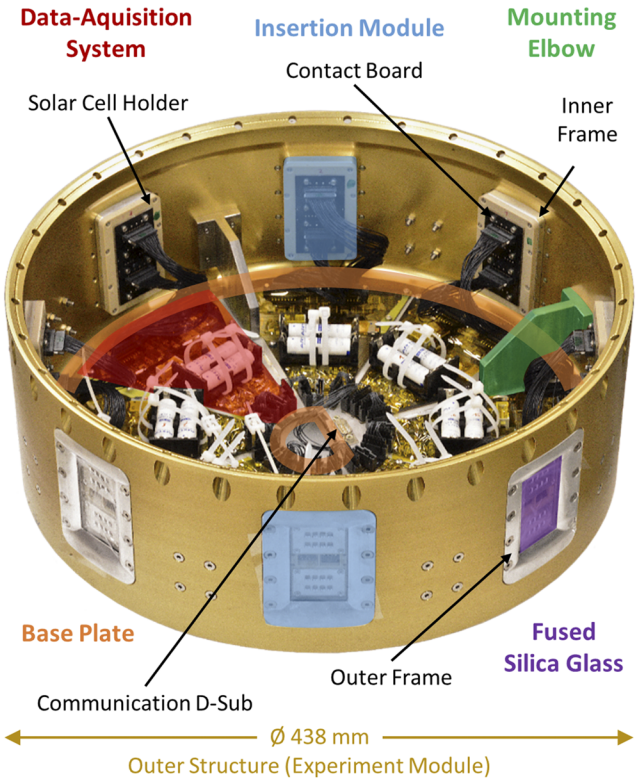

FIG. 1. OHSCIS experimental overview. Oblique-view photograph in the pre-flight configuration in Kiruna, Sweden, with colored assembly units: base plate (orange), mounting elbow (green), data-acquisition system (red), and insertion module (blue) with the fused silica glass (purple).

(JGS1), a material with exceptional mechanical strength and high transmission across the entire AM0 solar spectrum including the UV-region.[14] It is enclosed by the outer frame using Teflon© tape as a thin buffer layer and fitted to the inner frame using an O-ring sealing. The O-ring sealing absorbs shocks, vibrations, and compensates mechanical material deformations and heat-induced material expansion during flight.

The solar cell holder is a central part of the insertion module and is of particular importance for the entire experiment because it carries the scientific payload. It is made of polyether ether ketone (PEEK), a mechanically durable and heat-resistant polymer. The solar cell holder can be unscrewed from the inner frame to mount the solar cell modules. As a safety aspect, even in the case of a breaking window during flight, the robust PEEK material would withstand the conditions during reentry to protect the inside of the payload from hot-gas in-flow. Furthermore, PEEK acts as a thermal and electrical insulator to protect the solar cells from the hot ring mantle during ascent and reentry and to avoid electrical short-circuiting of the solar cells, respectively.

One solar cell module is fixed to the upper and one to the lower module position, respectively, by mounting the aluminum shadow mask on top of the solar cell modules as shown for the lower position in the bottom part of Fig. 2. The aluminum mask

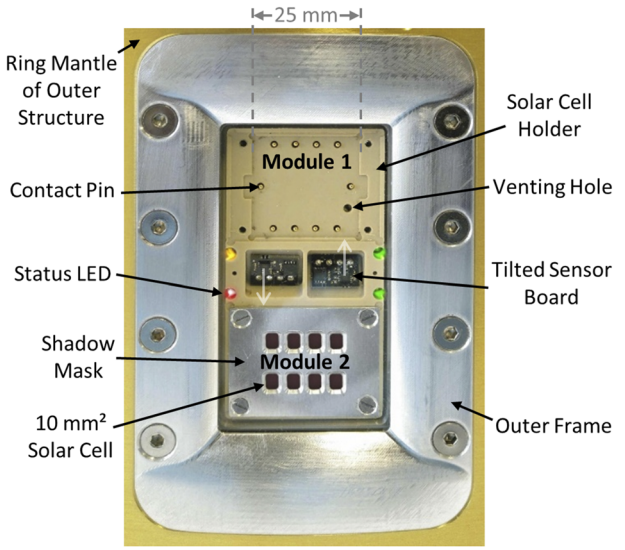

FIG. 2. Outside close-up view onto one of the eight hatches with the plugged-in insertion module. Behind the fused silica window (barely visible), the beige solar cell holder for two solar cell modules can be seen. At module position 1, the spring pins for solar cell contacts are visible, and in position 2, the shadow mask is assembled, defining eight solar cells with each 10 mm^2 aperture. Between the solar cell modules, two tilted sensor boards (one facing upward and the other facing downward, indicated with the white arrows) are placed to collect illumination and temperature information.

also defines the apertures, i.e., the illuminated area of the eight individual solar cells of a single module. Indentations on the backside of the aluminum masks keep the solar cells in the correct position during mounting and increase mechanical fixation of the cells to avoid possible scratching of the metal electrodes during mounting. This also decreases further the solar cell distance to the fused silica window. The entire mechanical layout is designed to minimize the distance between solar cells and the outer mantle radius to minimize shadowing effects onto the solar cells, e.g., the shadow masks have a distance to the fused silica of less than 1 mm.

In the middle of the solar cell holder, two small boards are placed, each carrying temperature (*MAX31725*) and light (*BH1750FVI*) sensors (Fig. 2). Those are tilted with an angle of 22.5° with respect to the solar cell surface, forming a relative angle of 45° between each other. Here, we note that this is the same angle as provided by the eightfold azimuthal symmetry of neighboring insertion modules. The four LEDs (two for status and two for 3.3 and 5 V power supply display) are located on the printed circuit board (PCB) attached to the backside of the solar cell holder (right side in Fig. 3). Viewing-channels in the solar cell holder allow to look down to these LEDs and pressurize the void volume of the insertion module to the inside of the rocket. The PCB on the backside of the solar cell holder further carries spring pins to contact the solar cell electrodes. A mounted solar cell module presses all spring pins to the same deflection and thereby reaches the same pressure at each pin to ensure reliable, low-Ohmic electrical contacts.

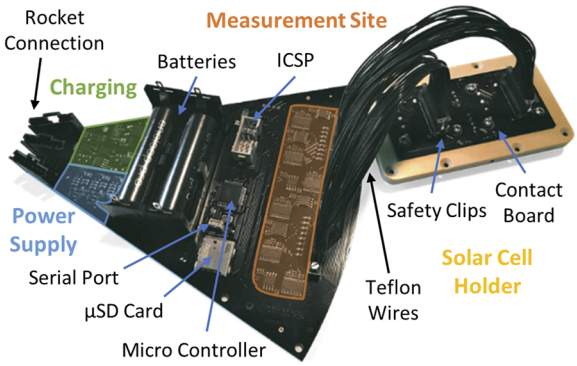

FIG. 3. Photograph of a complete single DAQ system. The black pizza-slice-shaped PCB contains spatially separated electrical units of different purposes that are colored. The solar cell holder on the right is seen from the backside and connected via two snap-in connectors.

III. ELECTRONIC DESIGN

The eight identical DAQ systems are located on pizza-slice-shaped PCBs to efficiently utilize the space inside the ring segment. In Fig. 3, we show a photograph of one complete DAQ system on a PCB with colored highlighting of the system's partitioning of the electric circuit, together with a connected solar cell holder. Each DAQ includes batteries, microcontroller (μC), and data storage and receives the service module signals. The design of the DAQ system strictly follows the KISS principle to keep it straightforward and simple, resulting in a system including many features to increase resiliency. A successor of this DAQ system has been used for deployment and long-time monitoring of the STRAWb experiment in the Northern Pacific. The DAQs are designed on black PCBs and fixed on top of the base plate with an intermediate layer of Rogers© foil to ensure electrical insulation and thermal conduction to the bottom plate. The black color aims to provide increased radiative thermal coupling to the surrounding, i.e., to radiate heat away more efficiently.

A schematic overview of the DAQ system architecture is given in Fig. 4, and a listing of the main electrical components can be found in Table I. The DAQ is powered by two AA 1.2 V NiMH batteries, which provide sufficient energy for several hours of operation. A DC/DC converter together with a dedicated charging circuit allows safe recharging of the system during the standby phase. During operation, the battery voltage is split into three independent power rails via highly efficient DC/DC converters, followed by LDO regulators to suppress high-frequency noise from the DC/DC converters. The main element of the DAQ is an 8 bit ATmega644PA **µ**C. The environmental sensors as well as a chip for voltage/current consumption monitoring are connected to the μC by I2C. An SPI bus controls the solar cell measurement system (details in Sec. IV) and carries the main data load during flight with fast and efficient data transfer. The rocket interface is implemented by optocouplers adapting the DLR design guidelines and allows one-way communication from the service module to the experiment. The in-flight signals of the service module are transferred to the inner pins (snap-in connectors), from where they are distributed to all eight identical DAQs.

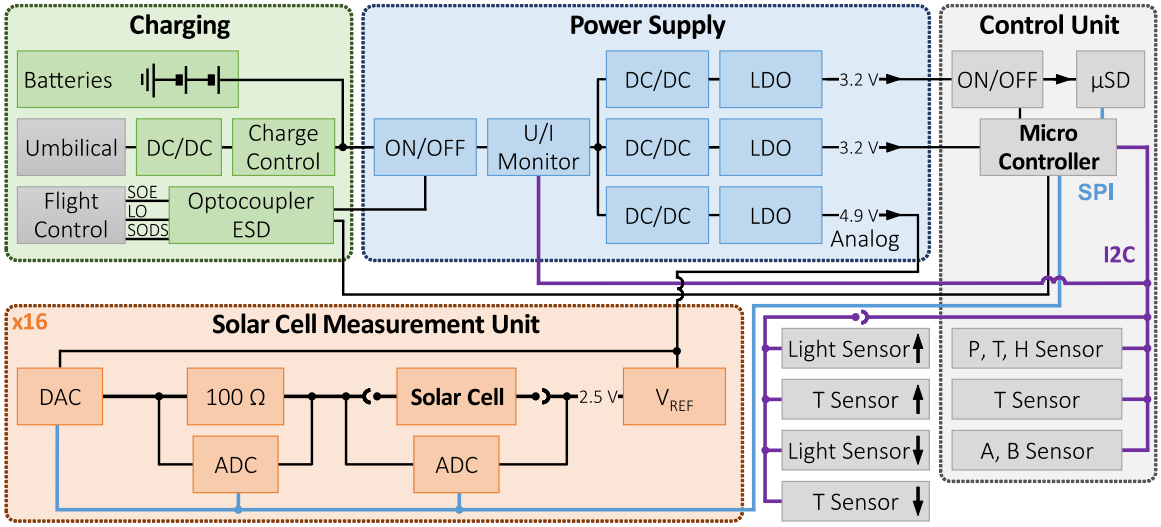

FIG. 4. Electrical system overview of each DAQ. The logical blocks can be divided into charging, power supply, control unit, and solar cell measurement unit and are colored in accordance with Fig. 3.

TABLE I. Main electrical components used in every single DAQ.

Components (number)	Model	Task	Features
Voltage reference (2×)	ADR431	Define virtual ground potential 2.5 V	Source/sink max 30/20 mA, high precision
Digital-analog converter (2×)	AD5676R	Sweep voltage to apply solar cell bias	16 bit, 15 mA sink, buffered output
Analog-digital converter (6×)	AD7193	Measure voltages at solar cell and shunt resistor	24 bit, gain 1, 8 fold oversampling and mean value calculation
Shunt resistor (16×)	APC1206	Enable high precision current measurements	0.01% tolerance, limiting short-circuit current
Microcontroller (1×)	ATMEGA644PA	Control DAQ, I2C and SPI communication, data handling	11.0592 MHz, 4 kB RAM
DC/DC converter (1×)	LMZM23601, TI	Convert charging input to 5 V system voltage	V_{out} = 5 V (max dropout 2 V), V_{in} ≥ 7 V for flexible charging
Charge controller	LTC4060, linear	Charge management for batteries	Simple configuration by pin strapping
Batteries (2×)	VHAA LT 1700 CFG, arts	Rechargeable power supply during flight	NiMH military-grade, vacuum, and acceleration stability
Boost converter (3×)	TPS61322XX, TI	Convert battery voltages to system voltages of 1 × 3.3 V and 2 × 5 V power rails	6.5-μA quiescent current, 1.8-A switch current boost converter, efficient drain of batteries
Low-dropout regulators (3×)	TPS73601	Reduce high-frequency signal in power rails	Low dropout 75 mV at full load
U/I sensor (1×)	INA219, TI	Monitor DAQ system power consumption	Autonomous measurements
Acceleration and magnetic field sensor (1×)	MC6470	Collect acceleration information	PCB bottom plate, three axes measurements
Temperature, humidity and pressure sensor (1×)	MS8607	Collect environmental information	PCB bottom plate
Temperature sensor (2× + 1×)	MAX31725	Collect temperature information	Sensor boards between solar cells, PCB bottom plate
Light sensor (2×)	BH1750FVI	Collect illumination information	Sensor boards between solar cells, adaption of sensor integration time

Using a specialized bootloader, the integrity of the program is ensured, as well as golden image reflash in the case of a μC FlashROM corruption during flight. The attached micro secure digital memory (μSD) card is supplied by a dedicated power rail to minimize power supply drops caused by write access to the file system. An integrated watchdog surveils the correct operation of the program and takes care of rebooting the system in the case of a software failure (as well as logging such failures for later analysis). The main program enables timeline logging with granularities of 93 μs and 10 ms, to ensure synchronization between the eight DAQ systems on the bottom plate.

The DAQ system monitors power consumption, temperature, humidity, and pressure on the PCB to provide basic environmental information inside the ring segment. Acceleration and magnetic field values (both in three axes) are also recorded during the measurements and provide a further option to synchronize the solar cell measurements of different segments post flight. In addition, the temperature and light sensor data on the solar cell holder are frequently recorded.

The heart of the experiment is the electrical characterization of the solar cells. A schematic overview of the measurement principle is presented in Fig. 4. The DAQ system consists of two high precision analog-to-digital converters (ADCs) (24 bit, internal oversampling), a constant voltage reference, and a digital-to-analog converter (DAC) (Fig. 4). The voltage reference provides a nominal voltage of 2.5 V as "virtual ground" to the solar cells. A high precision resistor of (100 ± 0.01) Ω acts as a shunt for the current measurement while protecting the DAQ system in the case of a short circuit inside one of the solar cells. The potential applied across the solar cell is defined by a DAC with an output range between 0 and 5 V. With the virtual ground potential of 2.5 V, negative and positive voltages can be applied to the measurement circuit. Consequently, solar cells of different polarities can be measured in both forward and reverse directions. This approach simplifies the design of the DAQ circuit and allows using standard electrical components that work without negative auxiliary voltages. While the DAC applies a voltage to the circuit, the first ADC measures the voltage drop across the solar cell, referenced to the 2.5 V source. At the same time, the second ADC records the voltage across the high precision resistor. The voltage is converted via Ohm's law, providing information about the amount of current flowing, as well as the direction. To accommodate for connector and cable resistances, four-point measurements are applied in the DAQ system.

IV. SOLAR CELL MEASUREMENT CYCLE

To maximize the number of measurements during the flight, two identical measurement circuits are used in parallel to simultaneously characterize two solar cells, one of each solar cell module. Herein, solar cells are characterized by sweeping the voltage across the solar cell in both directions, first from negative to positive voltages (forward) and subsequently from positive to negative voltages (backward). Measuring the I–V characteristics in both directions is important for solar cells exerting significant hysteresis, which is well known for perovskite solar cells, especially in the case of rapid voltage sweeps.[15] In the following, we discuss the file structure and data-writing in detail, since it strongly determines the data acquisition routine described thereafter.

The data storage is organized in a chunk structure. Each part of the data recorded is marked by a chunk byte, defining the logical content of the data chunk, and a second byte, carrying information about the length and internal unit of data stored. This allows a simple unpacker to handle data, even in the case of changes to the data stored inside the file (like adding or removing data chunks). This storage method automatically yields a small file size per measurement cycle, minimizing the risk of data loss in the case of unexpected reboots during the measurement phase. In addition, a dedicated directory is used to store datasets, driven by the start-of-experiment (SOE) signal. Overwriting of files is efficiently prevented, and no external access is needed between test cycles inside the launch tower.

To guarantee a defined timing during the measurement cycle, file operations on the μSD card have to be scheduled carefully. As a compromise between the available SRAM storage inside the μC and the step size in the sweep, a data block size of 512 bytes has been chosen. As a beneficial side effect, block writings of this size are realized efficiently on the μSD FAT32 file system.

In Fig. 5, a flowchart of the measurement is presented. A full measurement cycle starts with opening a file for the swept data. Next, the file size is expanded to the final size of the file (13 blocks of 512 bytes, 6.5 kB), allocating the necessary sectors inside the μSD card in advance. A first data buffer is prepared by the DAQ, containing all sensor data, as well as information about the directory and file number. All values necessary for the sweep run are calculated and also stored inside the first buffer. For MAPHEUS-8, the lower and upper voltages $V_L = -0.4$ V and $V_U = 1.35$ V are defined, respectively, and this range is covered with 240 equidistant steps for both forward and backward sweeps. The delay time between single steps is set to $\Delta t_D = 20$ ms, and an additional waiting time at the upper return point

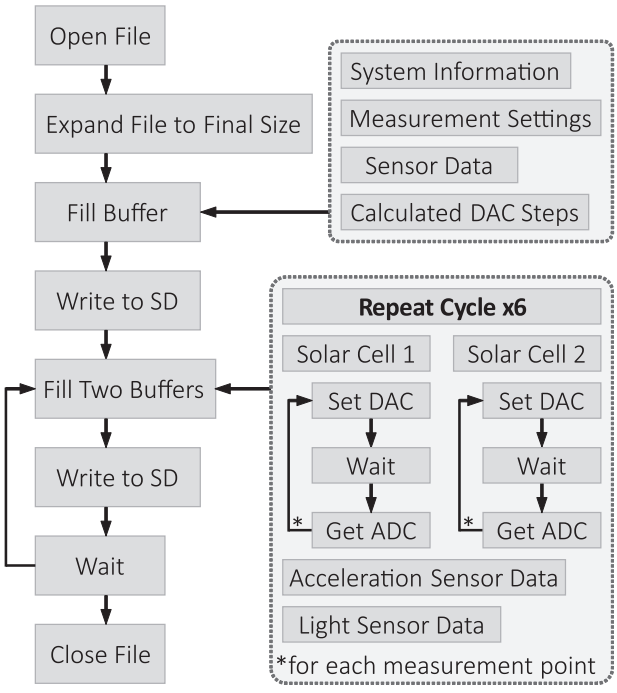

FIG. 5. Flowchart of the measurement and data-flow organization.

V_U is Δt_W = 200 ms. We used these identical parameters for all solar cell measurements, but in principle, the DAC voltages can be controlled separately to measure, e.g., solar cells of different polarities in the same solar cell holder. Here, we note that these voltages are applied by the DAC to the measurement circuit, i.e., solar cell and high precision resistor in series, with respect to the virtual ground. The voltage drop measured at the solar cell does not depend solely on this external bias but also on the photo-generated current of the solar cell. The photo-current is drained into the DAC via the shunt resistor, causing a voltage drop that effectively pulls up the potential of the solar cell electrode connected to the resistor. Therefore, we set V_L low enough to measure the full I–V characteristic in the fourth quadrant including the short-circuit current of the solar cells also during strong solar AM0 illumination.

For efficient use of the data blocks, the solar cell measurement is split up into six parts, three parts for the forward sweep and three for the backward sweep, where each part consists of 80 measurement points. The parts are executed successively in a loop. At the beginning of each part, two data buffers (one for each solar cell) are prepared, and the light and temperature sensor data from the solar cell holder are written to the SD card. The remaining free space in the buffers is then filled with sweep data. For each data point, a new (pre-calculated) DAC value is set, the constant time-delay Δt_D applied to allow voltages to settle, and then ADC data for both the shunt resistor voltage and the solar cell voltage are measured. The internal oversampling of the ADC is used to reduce noise to a reasonable level. After filling the two buffers, the defined delay Δt_D is applied until repeating the loop with the next part of the sweep. This delay is used to write the block of acquired data from the buffers to the μSD card, while the delay is dynamically adjusted to compensate for the time needed to write the data block. In other words, the time necessary for data-writing is counted to ensure equidistant time steps between the measurement points despite the splitting up of measurements into blocks. After finishing the loops, the DAC pins are set to high impedance, the file is closed, and the DAQ system is prepared for the next sweep of the following two solar cells.

V. OPERATIONAL TESTS

The mechanical stability and environmental stability of the experiment and measurement system have been tested in advance of the flight. To test mechanical stability, the entire module performed a shaking test in flight configuration with acceleration sensors attached to the experiment to monitor the accelerations at different module positions. The results reveal a significant resonance at low frequency (~200 Hz) of the bottom plate, leading to strong accelerations in the central region. However, at higher frequencies of 1 kHz and above, i.e., at frequencies where typically strong engine vibrations occur, resonances are suppressed in the central region of the bottom plate. In the course of the shaking, the entire experiment has been switched on to test the vibrational stability of the electronics, especially of the batteries for the power supply. Similarly, during the bench test, the switched-on experiment has been shaken together with the entire payload. These tests have proven the mechanical and electronic integrity of the experiment for the sounding rocket flight.

Due to the absence of convective cooling in space, thermal management via heat conduction is important to ensure a controlled temperature of the electronics during operation. The electronics dissipate heat to the aluminum bottom plate, hereby acting as a heat sink. To electrically insulate but thermally connect the DAQs to the plate, a thin layer of Rodgers© foil is inserted between the two parts. To test the concept of passive cooling, one complete DAQ system with a correspondingly sized aluminum bottom plate has been inserted into a vacuum oven and preheated to 65 °C. We simulated space conditions at a pressure of ~1 mbar to limit convective cooling and a temperature of ~65 °C for 10 min. This temperature has been chosen in the test because we expected the bottom plate to reach this maximum temperature due to thermal conduction via the mounting elbows from the outer structure in the course of the flight. The DAQ operated during the entire test and collected sensor data as well as sweep measurements nominally.

Various scenarios have been tested to improve the defined handling during unexpected occurrences. These include different malfunctions such as instantaneous power-loss, brown-out detection, loss of service system signals, the connection loss of sensors, μSD, and solar cells. Via detailed analysis of the system state during the tests and the data on the μSD afterward, we have optimized the exception handling on the software side to ensure reproducible behavior. This will allow for a full timeline reconstruction in any case—for time synchronization of the data and therefore parallelization after the flight. A long-term test has shown that the maximum operation time can reach more than 12 h. Even in the case of countdown prolongation, OHSCIS has enough power resources, consequently recharging in the launch tower is not mandatory, reducing external requirements. A key challenge in solar cell measurements is reliable electrical contacting. Already in the laboratory, there are various challenges to reach a reproducible, low-Ohmic contact between the electric measurement device and the nm-thin metal pads used as top electrodes for the solar cells. Regarding the strong vibrations and g-forces during launch, stable and immovable contacts are crucial to protect the metal pads and ensure electrical contacts. Because of the late access mounting of the solar cell modules, no rigid electrical contacting is possible. Therefore, the solar cell modules press onto gold-coated spring pins close to full stroke to maximize the grip between the pin and metal pad. We have conducted a shaking test of a single solar cell holder mounted with test modules to simulate the launch vibrations to the solar cell contacts. Test modules have been Ohmic resistances in the solar cell module layout, coated with a transparent conductive electrode and evaporated metal contact pads. The resistances before and after the test have been measured and no systematic change of the resistances occurred. In addition, optical microscopy did not reveal any scratching of the contact pins on the metal surface caused by the shaking.

To test the solar cell measurement circuit and to investigate the measurement precision of the DAQ system, we compared the DAQ measurements to the laboratory measurement device, consisting of a Keithley 2611B. We mounted a Si-photodiode (*BPW24R*) to the laboratory solar source to obtain defined and stable illumination. The diode has a highly stable I–V characteristic within a voltage and current range comparable to the solar cells. In Fig. 6(a), we show a photograph of the experimental realization of these validation measurements. Through four-point contacting, the diode was electrically connected alternatingly to the OHSCIS DAQ and also to the Keithley, a laboratory measurement device usually employed for electrical characterization of solar

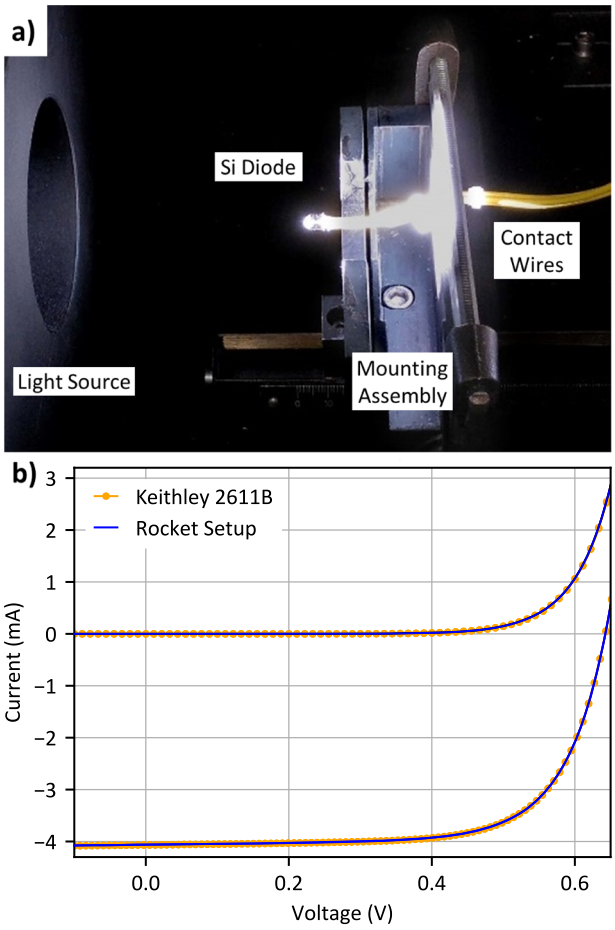

FIG. 6. Validation of the DAQ measurement system with a stable silicon diode. (a) Photograph of the laboratory experiment. (b) Resulting measurements of illuminated (lower) and dark (upper) measurements of the Si diode obtained with laboratory (yellow points) and rocket (blue line) measurement systems. For both systems, forward and backward sweeps are shown but are not distinguishable.

cells. For both measurement systems, dark-current and illuminated measurements were acquired under laboratory solar simulator illumination with a Xenon lamp with 1 sun (AM1.5g). The temporal and spectral stability of the light source of the source is A classified according to IEC 60904-9 Ed. 2.0, i.e., the short-term temporal intensity variability is within 2%.

For the dark-current measurements, the hatch was closed to avoid any scattered light from reaching the Si diode. For the illuminated measurements, a waiting time of several minutes let the diode reach temperature equilibrium to minimize thermal influences on the diode characteristics. In Fig. 6(b), we present I–V diode characteristics collected with the DAQ (rocket setup) and the Keithley (laboratory setup), respectively. Both have been measured forward and backward, for dark and illuminated conditions. The deviation of both measurement systems is negligible within the experimental error. The maximum absolute differences of the short-circuit current and the open-circuit voltage are 5 μA and 0.2 mV during illumination, respectively, which is in the low per mil range of the measured value. Assuming an ideally stable light source and the Keithley to produce ideal measurements, this measurement deviation underlines the high precision of the DAQ system for excellent solar cell measurements during the sounding rocket flight.

To further quantify the measurement precision of the DAQ system, we collected I–V measurements of a (100 ± 0.01) Ω resistor, fitted the measurements with a least-squares approach, and obtained a resistance of 100.03 Ω from the inverse slope. By relating fit and measurement values, we calculate the sample standard deviation of the current measurements σ_I = 0.057 μA. Here, the test resistor has the same resistance as the shunt resistor, thereby resulting in a similar contribution of read-out noise of both ADCs to the measurement error estimation. In other words, this value can be considered as an upper limit of the standard error in the determination of the short-circuit current, since voltage read-out noise at the shunt resistor has a negligible contribution on the current measurement in short-circuit conditions. Equivalently, the voltage standard error of open-circuit measurements is determined by the read-out noise of the shunt resistor, for which we derive an upper limit of $\sigma_V = \sigma_I \times 100\ \Omega = 5.7\ \mu$V.

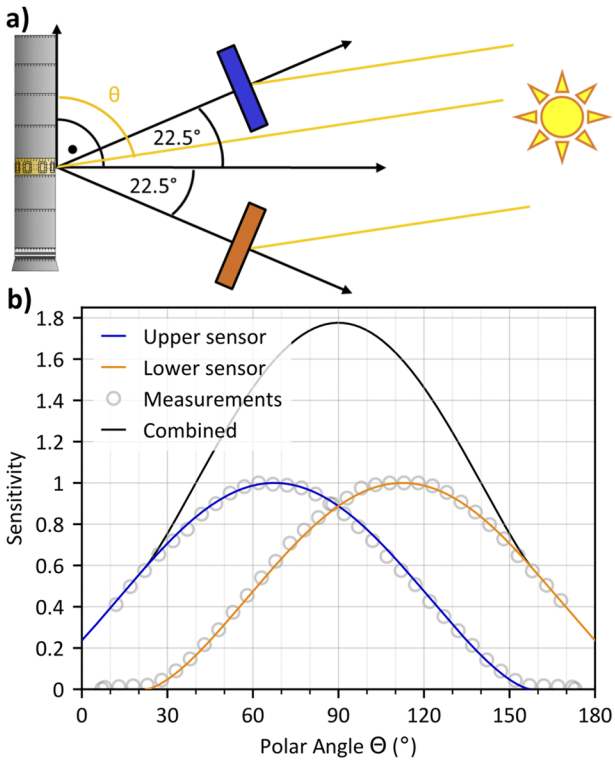

FIG. 7. View direction of the light sensors. (a) Schematic presentation of the orientation of the light sensors with respect to the solar cell surface normal. One sensor is facing slightly upward (blue) and one is facing downward (orange). (b) The angular sensitivity curves of the light sensors. Gray circles are laboratory test measurements, which can be approximated with analytical functions (colored lines) within a presumed measurement accuracy of five degrees. Taking the response function of both sensors together, their sum behaves like a single light sensor facing toward θ = 90°, i.e., in solar cell surface normal orientation.

In between the solar cell modules, two tilted sensor boards are located, one facing up and one facing down by 22.5° relative to the solar cell surface plane. Each sensor board has one I2C temperature sensor and light sensor (see Table I). These sensors are designed to provide detailed information about the temperature and illumination conditions as present for the solar cells located directly next to them. For the light sensors, we have adjusted the sensor integration time via the measurement time register to avoid saturation exposed to strong solar AM0 irradiation. In Fig. 7(a), we show a schematic drawing of the payload, together with the orientation of the tilted sensor boards. Summing up the angular response of both light sensors [Fig. 7(b)], the result is an angular response curve that peaks for normal incident light onto the solar cells. This way, a relative measure of the illumination strength and relative changes can be obtained.

The arrangement of the light sensors of 45° relative to each other allows estimating θ of the incident solar light direction by considering the differences in the measured illumination. In Fig. 7(a), the blue light sensor would receive more sunlight, resulting in a stronger response than measured by the orange sensor. The 45° also reflects the experimental symmetry of 45° between the eight windows. Parallelization of the light sensor data recorded by all eight DAQ systems enables the reconstruction of the solar position, which in turn allows deriving the irradiation intensity reaching the solar cells for power conversion efficiency analysis.

VI. FLIGHT EXPERIMENT PROCEDURE

A few hours before start, we mounted the solar cell modules into the solar cell holders and enclosed the solar cell holder with the outer window frames to obtain the complete insertion modules. During late access, the insertion modules were electrically connected via Samtec plugs with safety clips to the experiment module and integrated. At t − 7 min (before lift-off, LO), the SOE for OHSCIS was set, used to cycle power to the experiment. At regular system start-up, the μC initiated ADC calibration and switched thereafter in measurement mode, recording five complete dark-current measurements for each solar cell before LO. Once activated by the SOE, the DAQ system will work until shutdown by the low voltage lockout from the DC/DC converters to make sure that during flight, no accidental power-down is initiated.

At LO (t + 0 s), the internal clock started counting, while the measurements continued without any interruption. At t + 61 s, the rate-control system of the service module achieved a stable orientation of the payload, and thus, the main μg measurement time began. We allowed for a full measurement cycle of each solar cell until the start-of-data-storage (SODS) signal for OHSCIS was set at t + 155 s. Upon receiving the signal, the internal time stamp was saved and the ongoing sweep was completed and written to the SD card. Thereafter, an ADC re-calibration was initiated, and the calibration details were saved, and the measurement mode continued. During activated SODS, the sensor sensitivity of the gravitation sensors increased from a 16g range to a 2g range. We set the SODS off signal to t + 425 s, which was recorded together with an internal time stamp to have an additional external trigger for time synchronization of the eight DAQs.

The I–V measurements continued until the experiment shutdown was triggered by SOE off at t + 600 s. The onboard flight system safely switched off the DAQ system before payload touchdown for data protection.

VII. RESULTS

At payload recovery and disassembly, visual control of the experiment module confirms the full integrity of the mechanical parts, electrical parts, and solar cells. All eight glass windows are intact and also the electrical connection appears intact. Data extraction and conversion into ASCII files show that all eight segments steadily collected data and no exception occurred during the flight.

In Fig. 8, we show the recorded acceleration in the vertical direction of all eight DAQs covering the launch, main measurement time, and reentry. In the beginning, the acceleration phases of stages one and two are registered simultaneously by all eight segments, resulting in eight superimposed lines. At the strong reentry deacceleration at around 470 s, still, all eight DAQs show simultaneous acceleration measurements, indicating time synchronicity.

In more detail, the SODS signals are registered by all eight segments simultaneously, in particular, at SODS off, the internal clocks of all eight segments are within a range of 0.01 s. The measurement asynchronicity, i.e., the time difference of the start of single measurements in the eight segments, is limited to less than 0.7 s at this stage. This measurement asynchronicity presumably occurs due to cumulative time delays of single DAQs. These are caused by different write-access times of the very first buffer in each measurement, where no dynamic time adaption is used. The dynamic time adaption during the I–V acquisitions, however, prevents a larger total drift and guaranteed equidistant measurement acquisition within single solar cell sweeps in each segment.

The acceleration and light sensor data acquisitions both have a time-resolution of around 2 s, more than double of the maximum measurement asynchronicity and thus need no further fine-adjustment to be ideally parallelized. Therefore, all the sensor data and solar cell measurements acquired during the main measurement time are designated for in-depth analysis with parallelization and correlation of all the data obtained.

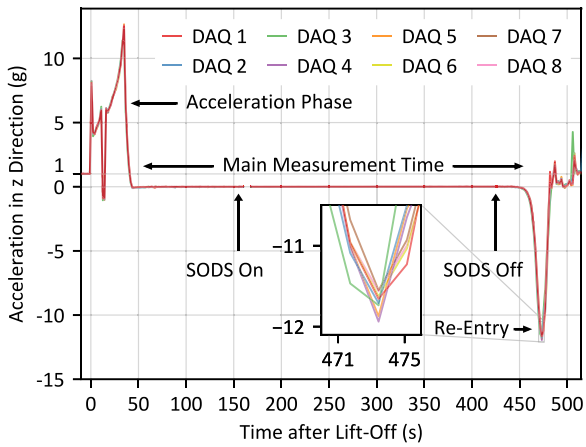

FIG. 8. Acceleration sensor data in the vertical direction of all eight DAQ systems. The most important timeline events for OHSCIS are labeled in the graph. The superimposed curves of the different DAQs prove the time synchronicity of the measurements.

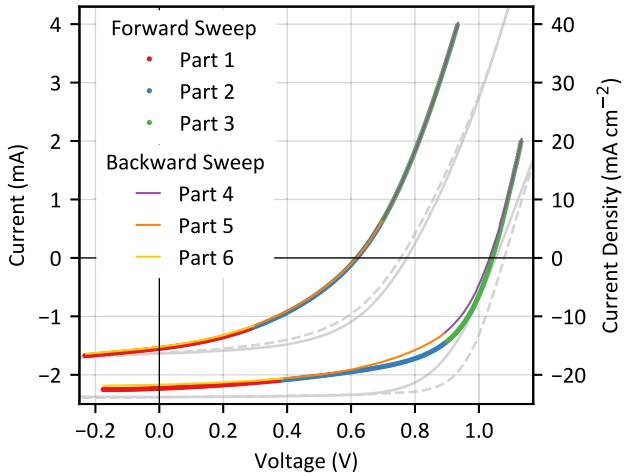

FIG. 9. Solar cell measurements at the end of the main measurement time beginning at t + 405 s collected at an altitude of more than 100 km for the segment with the strongest solar illumination at that moment (colored). The upper curves show the I–V characteristic of an organic solar cell and the lower curves for a hybrid perovskite solar cell. The colors allow distinguishing between different parts of the sweep measurement as they are collected in the buffer and written to the file. In addition, we show the corresponding reference measurements in laboratory conditions (1000 W cm^{-2}) of the same solar cell types from the same batch in solid gray (forward sweep) and dashed gray (backward sweep). A detailed analysis of solar cell measurements including all solar cell types and their response to different illumination conditions can be found in Ref. 13.

In Fig. 9, we present the example of solar cell measurements obtained at the end of the μg phase measured in one segment for an organic and perovskite solar cell from modules 1 and 2, respectively. Both solar cells show smooth I–V curves of diode-shape in both forward and backward sweep directions. These I–V curves and the low noise of the measurements allow us to assess the details of the measurement setup. In particular, there is a stable and reliable electrical contact for both solar cells and the DAQ performs as in the pre-tests (cf. Fig. 6). The system proves nominal operation from single DAC and ADC acquisitions, data collection, and storage up to post-flight retrieval of the data.

Both solar cells show clear diode-shaped I–V characteristics, proving the functionality of the charge-selective transporting layer. At the time of this measurement, the strongest solar illumination is detected for this segment with the photosensors, which is also supported by the strong photo-currents produced in both solar cells as seen by the vertical shift of the diode-shaped curves to negative currents. At this late stage of the flight, both organic and perovskite solar cells show a significant power generation. Therefore, after traveling to the launch site, mounting and waiting in the payload, being exposed to the harsh conditions with strong mechanical stresses during launch, and more importantly, after a time of nearly 6 min in μg space conditions in orbital altitudes they still function well.

The fourth quadrant, i.e., the region of negative currents and positive voltages, is covered completely for both solar cell types, together with the important axes intersections giving short-circuit current at zero voltage and open-circuit voltage at zero current. The minimum and maximum voltage drop measured across the solar cells depends on their photo-current response as described in the solar cell measurement cycle, Chap. 4. For the organic solar cell, the forward and backward sweeps are superimposed with barely visible differences. This highlights the stable payload orientation at this phase of the flight, resulting in stable illumination conditions during this measurement of around 10 s, being beneficial for an in-depth data evaluation. The perovskite solar cell measurement acquired at the same time shows hysteresis as manifested by the different shapes of the forward and backward sweep, which is well known from terrestrial I–V measurements. This hysteresis is most pronounced in the vicinity of the maximum power point, i.e., the solar cell operation point where the product of voltage and current and thus power extraction is maximal. This underlines the importance of characterizing perovskite solar cells in both forward and backward directions also under space conditions.

In Table II, we compiled an overview of environmental parameters (temperature and light sensor measurements) together with the solar cell key performance parameters. For completeness, we

TABLE II. Environmental and key performance parameters for the presented solar cell measurements.

Solar cell type	T (°C)	I (W m^{-2})	V_{oc} (V)	J_{sc} (mA cm^{-2})	FF (%)	V_{mpp} (V)	J_{mpp} (mA cm^{-2})	P_{mpp} (mW cm^{-2})	η (%)
In-flight									
Perovskite *m*-TiO_2, fw.	57	1214	1.04	22.32	59.3	0.81	16.97	13.79	11.4
PBDB-T:ITIC fw.	57	1214	0.62	15.49	39.2	0.37	10.03	3.75	3.1
Perovskite *m*-TiO_2, bw.	57	1200	1.03	21.69	56.6	0.76	16.70	12.67	10.6
PBDB-T:ITIC bw.	57	1200	0.62	15.22	39.0	0.37	9.83	3.66	3.0
Pre-flight									
Perovskite *m*-TiO_2, fw.	RT	1000	1.05	23.80	68.0	0.80	21.31	17.06	17.06
PBDB-T:ITIC fw.	RT	1000	0.77	16.39	54.0	0.54	12.68	6.85	6.85
Perovskite *m*-TiO_2, bw.	RT	1000	1.08	23.85	74.4	0.89	21.58	19.15	19.15
PBDB-T:ITIC bw.	RT	1000	0.76	16.32	50.7	0.51	12.23	6.25	6.25

included the results of the reference measurements in the laboratory, executed at standardized conditions, i.e., at room temperature (RT) and AM1.5g (1000 W m^{-2}). The maximum extracted power densities of the presented in-flight measurements are 3.75 and 13.79 mW cm^{-2} for the organic and perovskite solar cell, respectively. Based on the measured irradiation measured of around 1.2 suns, this converts to a power-conversion efficiency (η) of more than 11% and 3%, respectively. For more information, we refer the interested reader to our recent work "Perovskite and Organic Solar Cells on a Rocket Flight" based on the MAPHEUS-8 maiden flight.[13] In this work, a detailed description of all the solar cell types used, including their fabrication, reference measurements, and positioning in the OHSCIS experiment can be found. In addition, a comprehensive report and discussion of their electrical performance under different illumination conditions during this entire maiden flight is presented.

VIII. CONCLUSION

The design scope of simplicity and reliability has shaped the OHSCIS experiment presented in this work. Maximizing the experiment symmetry and thereby the chance of strong solar irradiation onto the solar cells by using eight similar cut-outs and DAQs enables the experiment to collect a high number of solar cell measurements and thus to use the limited time of flight efficiently for a high level of scientific insights. The one-way communication from the service module simplifies the maintenance before the start and during flight and maximizes the fail-safety on the software side. Accordingly, the electronic design is optimized for high data throughput while maintaining a high degree of resilience. For the electrical characterization of the solar cells, noise is suppressed and adaptive timing guarantees precise measurements. The measurement data are complemented with detailed monitoring of temperature and irradiation parameters to derive a full picture of the environmental conditions present for the solar cells.

The experiment passed all pre-tests and performed the flight onboard MAPHEUS-8 successfully without any defect. The analysis shows that data acquisition was successful during the entire flight for all eight segments and that the data are time-synchronized. The mechanical design avoided thermal stress for the DAQs and protected the solar cells, which were measured nominally and prove operational by generating power until the end of the μg phase.

OHSCIS was recovered completely and no experiment modifications are needed for future sounding rocket flights. The versatile design allows us to easily adapt the experiment to solar cells of different polarities or measurement requirements as well as different solar cell layouts. This offers the possibility to investigate the suitability of further novel material solar cell types for their use in space. Therefore, it provides an ideal test platform for all kinds of solar cells on future flight experiments.

ACKNOWLEDGMENTS

Financial support from Deutsche Forschungsgemeinschaft (DFG, German Research Foundation) under Germany's Excellence Strategy-Grant No. EXC 2089/1-390776260 (e-conversion) and by International Research Training Group 2022 Alberta/Technical University of Munich International Graduate School for Environmentally Responsible Functional Materials (ATUMS) as well as from TUM.solar in the context of the Bavarian Collaborative Research Project "Solar Technologies Go Hybrid" (SolTech) is acknowledged. We thank the department Base Mobile Rocket (MORABA) of the DLR Space Operations and Astronaut Training for the support and guidance during the project. We thank Dr. Roman Gernhäuser for the helpful suggestions throughout the project. We thank Dr. Christian Fruck for helping us with 3D-printed prototyping in the design phase. We thank all the various TUM-workshops, especially Reinhold Funer, and the central technology lab (ZTL) involved in the manufacturing of the hardware. We thank Lucas Krempel for his pioneering work on the solar cell measurement principle employed in this experiment.

DATA AVAILABILITY

The data that support the findings of this study are available from the corresponding author upon reasonable request.

REFERENCES

[1] G. Li, R. Zhu, and Y. Yang, Nat. Photonics **6**, 153 (2012).
[2] J. Hou, O. Inganäs, R. H. Friend, and F. Gao, Nat. Mater. **17**, 119 (2018).
[3] M. Grätzel, Nat. Mater. **13**, 838 (2014).
[4] M. A. Green, A. Ho-Baillie, and H. J. Snaith, Nat. Photonics **8**, 506 (2014).
[5] M. A. Green, E. D. Dunlop, J. Hohl-Ebinger, M. Yoshita, N. Kopidakis, and X. Hao, Prog. Photovolt. Res. Appl. **29**, 657 (2020).
[6] M. Kaltenbrunner, M. S. White, E. D. Głowacki, T. Sekitani, T. Someya, N. S. Sariciftci, and S. Bauer, Nat. Commun. **3**, 770 (2012).
[7] S. Kang, J. Jeong, S. Cho, Y. J. Yoon, S. Park, S. Lim, J. Y. Kim, and H. Ko, J. Mater. Chem. A **7**, 1107 (2019).
[8] I. Cardinaletti, T. Vangerven, S. Nagels, R. Cornelissen, D. Schreurs, J. Hruby, J. Vodnik, D. Devisscher, J. Kesters, J. D'Haen, A. Franquet, V. Spampinato, T. Conard, W. Maes, W. Deferme, and J. V. Manca, Sol. Energy Mater. Sol. Cells **182**, 121 (2018).
[9] D. Schreurs, S. Nagels, I. Cardinaletti, T. Vangerven, R. Cornelissen, J. Vodnik, J. Hruby, W. Deferme, and J. V. Manca, J. Mater. Res. **33**, 1841 (2018).
[10] Y. Tu, G. Xu, X. Yang, Y. Zhang, Z. Li, R. Su, D. Luo, W. Yang, Y. Miao, R. Cai, L. Jiang, X. Du, Y. Yang, Q. Liu, Y. Gao, S. Zhao, W. Huang, Q. Gong, and R. Zhu, Sci. China: Phys., Mech. Astron. **62**, 974221 (2019).
[11] S. Guo, C. Brandt, T. Andreev, E. Metwalli, W. Wang, J. Perlich, and P. Müller-Buschbaum, ACS Appl. Mater. Interfaces **6**, 17902 (2014).
[12] Y. Jiang, S.-C. Yang, Q. Jeangros, S. Pisoni, T. Moser, S. Buecheler, A. N. Tiwari, and F. Fu, Joule **4**, 1087 (2020).
[13] L. K. Reb, M. Böhmer, B. Predeschly, S. Grott, C. L. Weindl, G. I. Ivandekic, R. Guo, C. Dreißigacker, R. Gernhäuser, A. Meyer, and P. Müller-Buschbaum, Joule **4**, 1880 (2020).
[14] M. A. Green, Prog. Photovoltaics **20**, 954 (2012).
[15] H. J. Snaith, A. Abate, J. M. Ball, G. E. Eperon, T. Leijtens, N. K. Noel, S. D. Stranks, J. T.-W. Wang, K. Wojciechowski, and W. Zhang, J. Phys. Chem. Lett. **5**, 1511 (2014).